ChemSusChem

Research Article
doi.org/10.1002/cssc.202402576

Chemistry Europe
European Chemical Societies Publishing

www.chemsuschem.org

Hot Paper

Size-Dependency of Electrochemically Grown Copper Nanoclusters Derived from Single Copper Atoms for the CO Reduction Reaction

Keitaro Ohashi,[a] Kosei Nishimura,[a] Kaito Nagita,[a] Takuya Hashimoto,[a] Shoko Nakahata,[a] Takashi Harada,[a] Toshiaki Ina,[b] Shuji Nakanishi,*[a, c] and Kazuhide Kamiya*[a, c]

Electrochemically grown copper nanoclusters (CuNCs: <3 nm) from single-atom catalysts have recently attracted intensive attention as electrocatalysts for CO_2 and CO reduction reaction (CO_2RR/CORR) because they exhibit distinct product selectivity compared with conventional Cu nanoparticles (typically larger than 10nm). Herein, we conducted a detailed investigation into the size dependence of CuNCs on selectivity for multicarbon (C_{2+}) production in CORR. These nanoclusters were electrochemically grown from single Cu atoms dispersed on covalent triazine frameworks (Cu-CTFs). *Operando* X-ray absorption fine structure analysis revealed that Cu-CTFs containing 1.21 wt% and 0.41 wt% Cu (Cu(h)-CTFs and Cu(I)-CTFs, respectively) formed CuNCs of 2.0 and 1.1 nm, respectively, at -1.0 V *vs.* RHE. The selectivity for CORR products was particularly dependent on the size of CuNCs, with the Faraday efficiencies of C_{2+} products being 52.3% and 32.7% at -1.0 V *vs.* RHE with Cu(h)-CTFs and Cu(I)-CTFs, respectively. Spherical CuNCs modeling revealed that larger cluster sizes led to a greater proportion of a surface coordination number (SCN) of 8 or 9. Density functional calculations revealed that the CO dimerization reaction was more likely to proceed at SCNs of 8 or 9 compared to SCN of 7 because of the stability of the *OCCO intermediate.

Introduction

Excessive CO_2 emissions associated with the use of fossil fuels pose a substantial threat to the sustainable development of our society; hence, developing technologies that utilize CO_2 as an alternative carbon feedstock is crucial.[1–4] The electrochemical conversion of CO_2 into valuable fuels and chemical feedstocks is a promising approach to address the challenges of the carbon cycle.[5–7] However, for widespread societal implementation, improving various properties, such as product value, selectivity, reaction rate, and durability, is essential.[8–10] In particular, generating high-value multicarbon (C_{2+}) products such as ethylene, ethanol, and acetate for use as sustainable fuels and renewable feedstocks of carbon-based fine chemicals is highly desirable. Cu-based metal catalysts are well known for their efficiency in producing C_{2+} products though the dimerization of intermediate CO.[11–14] Consequently, numerous studies have focused on developing highly active and selective Cu-based CO_2 reduction reaction (CO_2RR) catalysts.

Single-atom Cu electrocatalysts have attracted significant attention because of their efficient and unique organic production activity, compared to conventional Cu nanoparticle (CuNPs) electrocatalysts larger than 10 nm.[15–19] Initially, single Cu atoms were believed to serve as the main active sites in these catalysts. Nevertheless, recent reports have demonstrated, with increasing consensus, that electrochemically *in-situ*-prepared Cu nanoclusters (CuNCs) derived from these single Cu atoms are responsible for the reduction of CO_2 to organics.[20–26] Wang and colleagues have reported that the CuNCs derived from Cu(II) phthalocyanine achieved a CH_4 Faradaic efficiency (FE) of 66%.[21] They used X-ray absorption spectroscopy (XAS) analysis to confirm that <2 nm Cu clusters were formed during CO_2 electroreduction. The CuNCs derived from copper-nitrogen-doped carbon (Cu–N–C) were active centers for the CO_2RR toward ethanol, with a Faradaic yield as high as 55%, and for the CO reduction reaction (CORR) toward C_2 products, with a Faradaic yield of 80%. Cuenya and coauthors recently conducted a detailed investigation of metal-nitrogen-doped carbon (*M*–N–C: *M* = Fe, Sn, Cu, Co, Ni, Zn) using *operando* X-ray absorption fine structure (XAFS) spectroscopy to examine changes in the active centers during the CO_2RR.[27] They found that all of their investigated catalysts except Ni–N–C reversibly formed metal clusters during the CO_2RR and that the CuNCs derived from Cu–N–C exhibited poor CO_2RR activity in their studies. Thus, the activity and selectivity of SAC-derived CuNCs vary dramatically across different studies.

[a] *Research Center for Solar Energy Chemistry, Graduate School of Engineering Science, Osaka University, Toyonaka, Osaka, Japan*
[b] *Japan Synchrotron Radiation Research Institute (JASRI/SPring-8), Sayo-gun, Hyogo, Japan*
[c] *Innovative Catalysis Science Division, Institute for Open and Transdisciplinary Research Initiatives (ICS-OTRI), Osaka University, Suita, Osaka, Japan*
Correspondence: *Prof. Dr. Shuji Nakanishi and Prof. Dr. Kazuhide Kamiya, Research Center for Solar Energy Chemistry, Graduate School of Engineering Science, Osaka University, Toyonaka 560-8531, Osaka, Japan.*
Email: nakanishi.shuji.es@osaka-u.ac.jp and kamiya.kazuhide.es@osaka-u.ac.jp

Supporting Information for this article is available on the WWW under https://doi.org/10.1002/cssc.202402576

We assume that the variation in activity arose from differences in the sizes of SAC-derived CuNCs. For example, Strasser and coworkers investigated the particle size dependence of the CO_2RR activity of CuNPs in the size range of 2–15 nm and found that smaller particles exhibited higher formation rate for H_2 and CO.[28] On the other hand, the size of SAC-derived CuNCs is expected to range from around 0.5 nm to at most 3 nm, which falls within a smaller size range than that of the CuNPs reported in the previous study. The formation of stable CuNCs is challenging, and these clusters are prone to structural changes during electrolysis. To gain deeper insights into C_{2+} production on SAC-derived CuNCs, it is essential to more thoroughly and systematically investigate their size-dependent activity under electrochemical conditions using *operando* techniques.

Toward that end, in the present work, we used single Cu-modified covalent triazine frameworks (CTFs) as the precursor for the CuNCs. Our group has demonstrated that metal modified CTFs (*M*–CTFs) serve as selective SACs for various reactions.[29–34] For example, Ni- and Sn-doped CTFs have proven to be effective electrocatalysts for the CO_2RR to CO and HCOOH, respectively.[35] Because metals can be loaded onto CTFs under ambient conditions without the need for high-temperature heat treatments, as required for *M*—N—C catalysts, the metal loading amounts in CTFs can be easily controlled. Moreover, the coordination structure of the SACs is expected to be relatively uniform. Additionally, as the CTFs support remains identical while only the metal concentration is varied, structural changes at the three-phase interface that serve as the reaction site for gaseous substrates are expected to be minimized. In the present study, we used *operando* XAFS to investigate the size of CuNCs derived from CTFs doped with desired amounts of Cu atoms and compared their size and reduction activity toward CO, which is a key intermediate in the production of C_{2+} from CO_2. In addition, we modeled the surface structure of CuNCs on the basis of their size and theoretically calculated their activity for C–C bond formation.

Results and Discussion

Characterization of Cu-CTFs

CTFs were prepared by polymerizing 2,6-dicyanopyridine in molten $ZnCl_2$ containing carbon nanoparticles, as reported in our previous paper.[29] We incorporated Cu atoms into the CTFs by impregnating the obtained CTFs in Cu^{2+} solutions (Figure 1a). Various Cu-CTFs with different Cu mass concentrations (Cu(h)-CTFs: 1.21 wt_{Cu}%, Cu(m)-CTFs: 0.74 wt_{Cu}%, and Cu(l)-CTFs: 0.41 wt_{Cu}%) were synthesized by adjusting the concentration of Cu^{2+} ions in the impregnation solution to 1.0, 0.4, and 0.2 mM, respectively. Table S1 lists the surface elemental composition of each Cu-CTF, as determined by X-ray photoelectron spectroscopy (XPS).

To evaluate whether Cu atoms are singly modified on the CTFs, we carried out high-resolution transmission electron microscopy (HR-TEM) (Figure S1). The primary particles of CTFs were ~40 nm and agglomerated to form secondary particles.

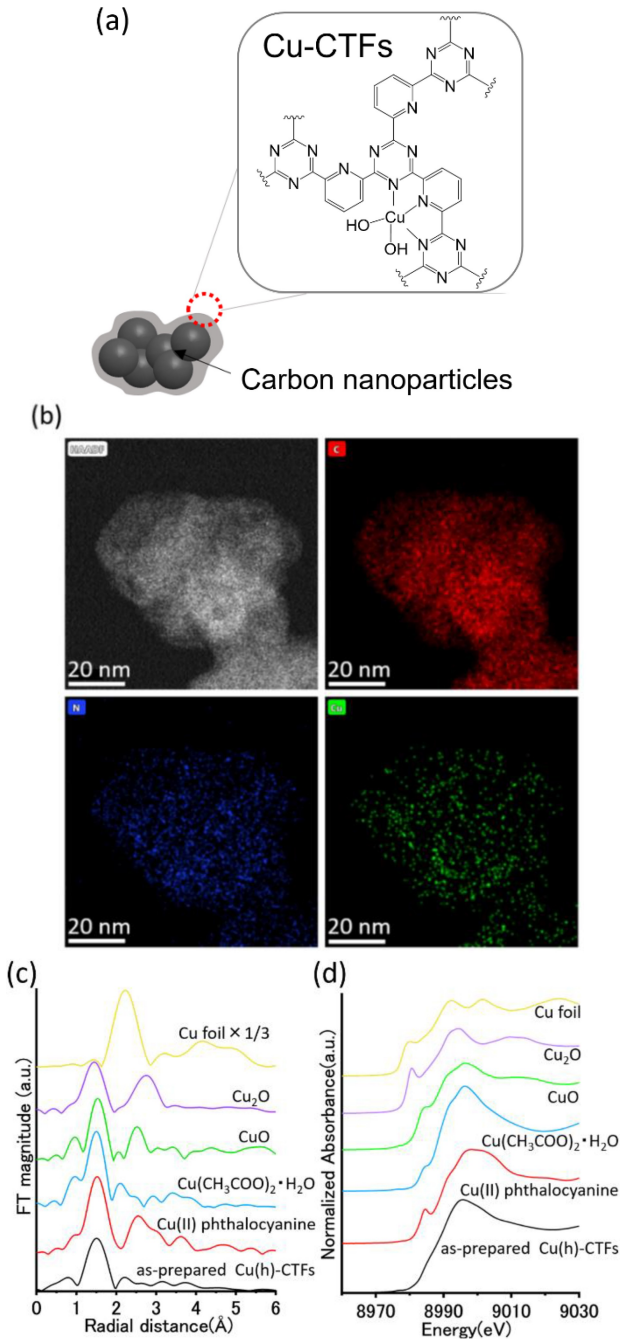

Figure 1. (a) Schematic of as-prepared Cu-CTFs hybridized with carbon nanoparticles. (b) Representative HAADF-STEM images of Cu(h)-CTFs and corresponding elemental mapping images for C, N, and Cu atoms. (c) The k^3-weighted FT-EXAFS and (d) XANES spectra of as-prepared Cu(h)-CTFs and reference samples.

No visible black spots, typically attributed to Cu particles, were observed. In addition, high-angle annular dark field scanning transmission electron microscopy (HAADF-STEM) inspections with elemental mapping images show that Cu atoms were homogenously dispersed on the platform (Figures 1b, S2, and S3). To finely explore the structure and coordination environment of the Cu-CTFs, we performed a Fourier transform of the k^3-weighted extended X-ray absorption fine structure (FT-

EXAFS) (Figures 1c and S4a). The peaks assignable to Cu–Cu (2.2 Å) or Cu–O–Cu (2.5 Å) were negligible, and only the peak derived from the first coordination sphere composed of light elements (Cu–N or Cu–O: 1.5 Å) was clearly observed. Overall, these evaluations indicate that Cu atoms were dispersed on the CTFs in a single state. The valence state of the Cu on the CTFs was investigated using X-ray absorption near edge structure (XANES) (Figures 1d and S4b) and X-ray photoelectron spectroscopy (XPS) (Figure S5). The Cu–K edge XANES spectra confirmed that the adsorption edge of the Cu-CTFs coincide with that of Cu^{2+} reference materials. We confirmed the specific satellite peaks of Cu^{2+} from the Cu 2p XPS spectra. Specifically, singly isolated Cu(II) atoms were dispersed on the CTFs. Field-emission scanning electron microscopy (FE-SEM) was performed to assess the morphological properties of the Cu-CTFs deposited onto a gas diffusion electrode (GDE) (Figure S6). A cross-sectional SEM image revealed that the catalyst layer on the microporous layer was approximately less than 0.5 μm thick.

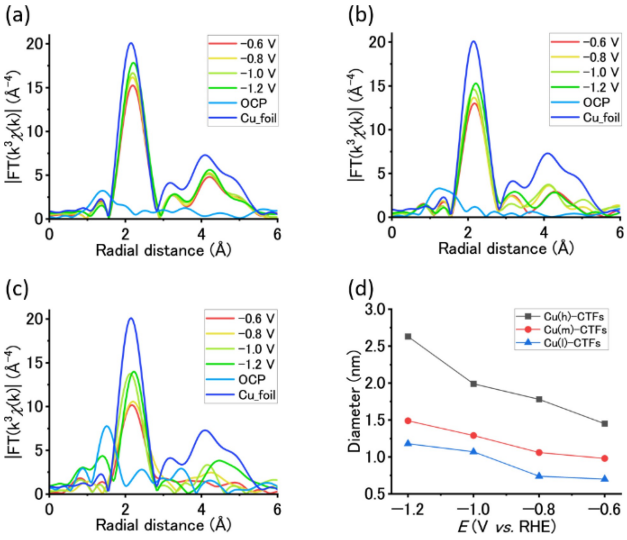

Figure 2. The k^3-weighted FT-EXAFS spectra under applied potentials from −0.6 V to −1.2 V *vs.* RHE and at OCP with (a) Cu(h)-CTFs, (b) Cu(m)-CTFs, and (c) Cu(l)-CTFs. (d) CuNCs size predicted on the basis of the coordination numbers obtained from FT-EXAFS results, plotted against the potential.

Operando XAFS Analysis

In the previous section, we confirmed that most of the Cu atoms were singly dispersed on the as-prepared Cu-CTFs. However, single-Cu-atom structures can aggregate, and such aggregates could potentially function as active centers during the CORR. Thus, before conducting the CORR test, we used *operando* XAFS to investigate the local structure of Cu atoms in Cu-CTFs under a negative potential in the presence of CO. For the *operando* XAFS measurements during gaseous CO electrolysis, a handmade three-chamber electrochemical cell was constructed, with two of the electrolyte compartments separated by Nafion (Figure S7). The gas chamber was sealed with Kapton tape, and X-rays were introduced through its window to the backside of the GDE to observe fluorescence X-rays. The changes in the EXAFS spectra stagnated 20 minutes after the potential was applied (Figure S8). Therefore, the following *operando* XAFS data were obtained 20 minutes after the start of electrolysis.

The XANES and EXAFS analysis results for each Cu-CTFs are shown in Figures S9 and 2a–c, respectively. Prior to applying the cathodic potential (i.e., under open-circuit potential (OCP) conditions), we confirmed that Cu existed primarily in the divalent state. In addition, we confirmed that Cu was in a single atomic state in all of the samples. Under −0.6 V *vs.* reversible hydrogen electrode (RHE), the Cu(II) was reduced to Cu(0) and a peak corresponding to Cu–Cu bonding was observed in the EXAFS spectrum (Figure 2a). Moreover, as a more negative potential was applied (i.e., from −0.6 V to −1.2 V *vs.* RHE), the intensity of the Cu–Cu peak increased. A similar trend was observed under an Ar atmosphere as under the CO atmosphere (Figure S10). Similar to our observations of the Cu(h)-CTFs, we observed that single Cu(II) sites were reduced to Cu(0) and that Cu aggregation grown from −0.6 V to −1.2 V *vs.* RHE for the Cu(m)-CTFs and Cu(l)-CTFs, respectively (Figures 2b and 2c). In the spectra of all of the investigated Cu-CTFs, the Cu–N bond peak almost disappeared. The Cu–Cu coordination numbers obtained from EXAFS spectra at each potential for each Cu-CTF are shown in Table S2. The Cu(h)-CTFs at −1.0 V *vs.* RHE were found to have a Cu–Cu coordination number of 9.7, whereas the Cu(l)-CTFs at −0.6 V *vs.* RHE had a coordination number of 5.8.

To estimate the size of the generated Cu clusters, we first modeled the clusters and calculated their corresponding coordination numbers (Figure S11; see Experimental section for details). The experimentally obtained coordination numbers were then incorporated into the fitting-curve equation to determine cluster sizes (Figures 2d and S12~S14). The fitting analyses showed that the Cu clusters derived from single Cu atoms grew larger as increasingly negative potentials were applied. Among the three Cu-CTFs, the Cu(h)-CTFs consistently formed the largest Cu clusters at each potential. Notably, at −1.0 V vs. RHE, Cu(h)-CTFs produced Cu clusters with a size of 2.0 nm, which is 1.8 times larger than those formed by the Cu(l)-CTFs (1.1 nm). The observed sizes of CuNCs should not be assumed to represent the thermodynamically most stable phase. Rather, they reflect the cluster sizes present during electrolysis. The limited growth of the clusters may be attributed to the low density of Cu atoms, which likely imposes kinetic limitations on further size expansion.

Intriguingly, when the OCP measurements were performed in air after electrolysis, the Cu–Cu peaks disappeared, indicating that CuNCs are unstable under OCP conditions (Figure S15). This observation aligns with the previously reported literature.[21] Detailed structural analyses of the Cu-CTFs after electrolysis are planned for future investigations.

CO Electrolysis Performance on CuNCs

We attempted to experimentally determine the CORR activity depending on the size of Cu clusters on the CTFs. Cyclic voltammetry (CV) measurements were conducted under both CO and Ar atmospheres (Figure S16). The onset potential was approximately −0.7 V *vs.* RHE for the bare CTFs, whereas it was −0.5 V *vs.* RHE for the Cu(h)-CTFs. Under Ar conditions, the current density at −1.2 V *vs.* RHE was 25 mA/cm^2 for the CTFs and 115 mA/cm^2 for the Cu(h)-CTFs. The reduction current of the Cu(h)-CTFs decreased upon CO addition, indicating that adsorbed CO suppressed the hydrogen evolution reaction (HER).

The CORR products in outlet gas streams from the gas chamber and electrolytes from the catholyte compartment were analyzed using gas chromatography (GC) (Figure S17) and ^{1}H nuclear magnetic resonance (NMR) spectroscopy (Figure S18) after constant-potential electrolysis, respectively. From Figure 3a, we obtained the FE of the CORR under a cathodic potential ranging from −0.6 V to −1.2 V *vs.* RHE in 1 M KOH for the Cu(h)-CTFs. The total FE for C_{2+} products at −1.0 V *vs.* RHE was 50.7%, with specific FE values of 22.0%, 2.5%, 10.4%, and 15.8%, for acetate, *n*-propanol, ethanol, and ethylene, respectively. By contrast, the FE for the C_1 product (methane) was 2.9%. When the applied potential was shifted from −1.0 V to −1.2 V *vs.* RHE, the FE_{C2+} decreased from 50.7% to 41.6% and the FE_{C1} increased from 2.9% to 10.0%. As discussed in the previous section, the size of the Cu clusters grown under cathodic potential varied depending on the degree of Cu modification on the substrates. To assess the potential effect of cluster size on the CORR activity, we conducted similar experiments using the Cu(m)-CTFs and Cu(l)-CTFs (Figures 3b, c and S19). The FE_{C2+} values were 40.2% for the Cu(m)-CTFs and 32.7% for the Cu(l)-CTFs at −1.0 V *vs.* RHE, both of which were lower than the value for the Cu(h)-CTFs. The FE_{C2+} values consistently increased with higher Cu loadings across all of the examined potentials, not just at −1.0 V *vs.* RHE. As shown in Figure S20, the onset potentials for C_{2+} and C_1 production were around −0.6 V and −0.7 V, respectively, and these values were independent of the catalyst used.

To further confirm the selectivity of C_{2+} products depending on the size of CuNCs, we analyzed the variation in the formation rate of C_{2+} products per unit of normalized surface area of CuNCs (SA_{CuNCs}, Table S3). The C_{2+}, C_1 and each C_{2+} product formation rates per unit of normalized SA_{CuNCs} are shown in Figures 3d, 3e and S21. The mean C_{2+} product yields for each experiment are summarized in Table S4. A greater than 3-fold difference in the normalized C_{2+} formation rate was observed between the smallest and largest sized CuNCs at each potential. Comparison of the normalized formation rates of each C_{2+} product in Figure S21 shows that the formation rates of acetate, ethylene and *n*-propanol were size-dependent for CuNCs. The normalized C_1 product formation rate, on the other hand, confirmed the absence of a size dependence for CuNCs. We also determined the turnover frequency for C_1 and C_{2+} formation based on the surface Cu atoms on CuNCs ($TOF_{surface\_Cu}$, Figure S22). For the $TOF_{surface\_Cu}$ calculation, the amount of total and surface Cu atoms relative to the spherical diameter of the modeled CuNCs are shown in Table S5. The $TOF_{surface\_Cu}$ for C_{2+} increased with larger CuNCs, whereas that for C_1 product remained almost unchanged. The $TOF_{surface\_Cu}$ for C_{2+} reached up to 7.2 s^{-1} at 2.6 nm of diameter of CuNCs. These findings confirm that the C_{2+} formation rate is dependent on the size of

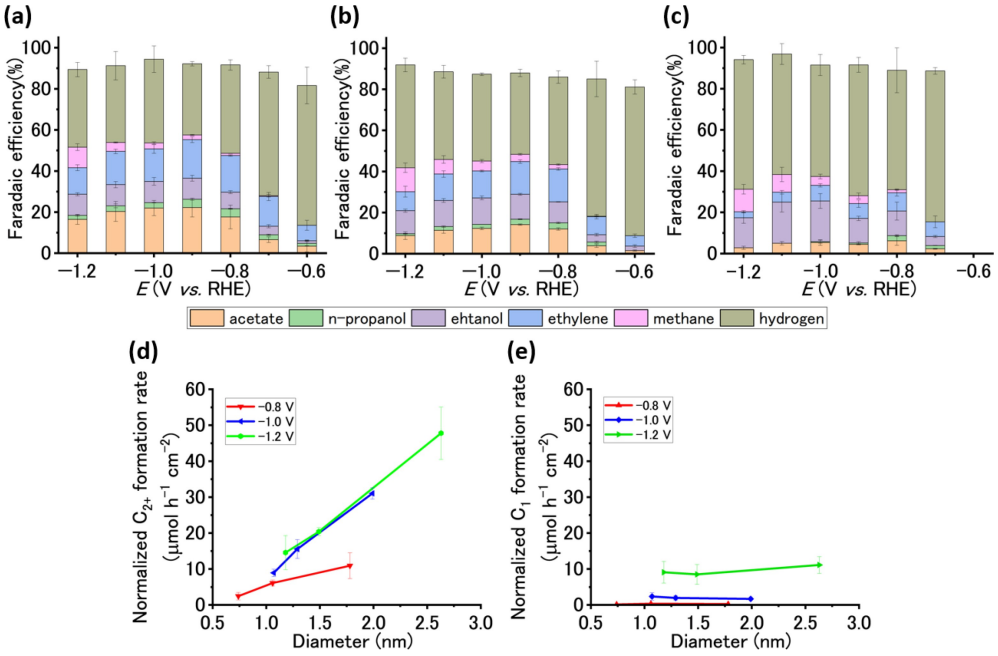

Figure 3. FEs of CORR products plotted against potential for (a) Cu(h)-CTFs, (b) Cu(m)-CTFs, and (c) Cu(l)-CTFs. (d) The formation rate of C_{2+} products and (e) C_1 product per unit of normalized SA_{CuNCs} against each size of CuNCs. The error bars represent the standard deviations obtained from three experimental trials.

the CuNCs and the larger size of CuNCs is more likely to possess a surface that can readily produce C_{2+} products.

In Figures 3a–c, the FE_{C2+} at −1.2 V *vs.* RHE was lower than that at −1.0 V *vs.* RHE for all three catalysts. To explore the mechanisms underlying the decrease in FE_{C2+} at −1.2 V *vs.* RHE, we plotted the polarization curves and total current densities (Figure S23). The $\log(j_{C2+})$ reached its maximum at −1.1 V *vs.* RHE for each Cu-CTF. This trend is likely due to the depletion of *CO, which constrains CO dimerization, consistent with previous analyses.[36–38]

Modeling CuNCs to Calculate Coordination Number for Surface Atoms

The coordination numbers for the surface-exposed atoms change depending on the size of the nanoclusters.[28,39] Herein, we modeled CuNCs in the size region suggested by the *operando* XAFS results to identify the structure of exposed Cu atoms that function as an active center for the CORR. Figure 4 shows the surface coordination number (SCN) distribution of CuNCs with sizes in the range 0.6–5 nm. Representative schematics of CuNCs are shown in Figures S11b and S11c. Sites with SCN <8 represent surface Cu atoms on either the step or the kink sites. According to the *operando* XAFS results (Figure 2d), Cu(I)-CTFs and Cu(h)-CTFs formed ~1.2 nm and ~2.6 nm CuNCs at −1.2 V *vs.* RHE, respectively. At a cluster size of 1.2 nm, the proportions of clusters with SCN $=8$ and SCN <8 were 14% and 85%, respectively. As the cluster size increased to 2.6 nm, the proportions shifted to 20% for SCN $=9$, 14% for SCN $=8$, and 66% for SCN <8. The overall trend showed a decrease in the proportions of sites with SCN <8 and an increase in those with SCN ≥ 8 as the cluster diameter increased. That is, larger clusters have a greater proportion of terrace surfaces compared with step and kink sites. Under the assumption that the change in the SCN of exposed Cu atoms influences the C_{2+} formation activity, we conducted a density functional theory (DFT) study, as described in the next section.

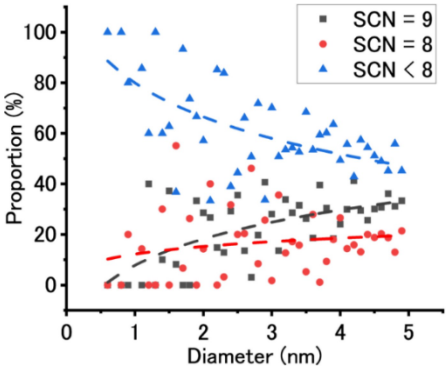

Figure 4. Proportions of surface coordination numbers (SCN $=9$, 8, or <8) on the modeled Cu clusters. The dashed lines represent the guidelines based on logarithmic fitting to trends in proportions.

DFT Study on CO Dimerization on Cu Sites with Various SCNs

C–C bond formation is a key step in the production of C_{2+} products in the CORR and CO_2RR. In general, C–C bond formation on bulk Cu proceeds through a Langmuir–Hinshelwood-type CO dimerization process.[40–42] In this process, two CO molecules adsorbed onto adjacent Cu atoms react to form an *OCCO intermediate. A recent report showed that C–C bond formation via CO dimerization occurs on CuNPs and oxide-derived copper.[43] Additionally, a mechanism for the CO dimerization on catalysts with several adjacent Cu atoms has been proposed.[44] Therefore, the CO dimerization is also assumed to be the key step for C–C bond formation on CuNCs. As discussed in the previous session, as the cluster size increases, the proportion of terrace sites with SCN $=8$ or 9 increases and the proportion of step sites with SCN <8 decreases. Herein, we investigated the CO dimerization activity at each site using DFT to identify the relationship between cluster size and C_{2+} production activity. We calculated the energy diagram for the CO dimerization reaction at different SCN sites using various facets (SCN $=9$: Cu (111), SCN $=8$: Cu (100), SCN $=7$: Cu (211)) by employing the climbing image nudged elastic band (CI-NEB) method. Given the hydrogen bonding stabilization of the oxygen atom in CO, we constructed models that include explicit water molecules. In addition, on the basis of a previous paper by Nørskov, we replaced one of the water molecules with a hydronium ion to represent a pseudo-negative potential on the bulk Cu.[41,45] Figures 5 and S24 show energy diagrams as functions of the C–C bond length between two CO molecules (d_{C-C}) and the optimized structure of the transition state (TS) (see Figures S25–S27 for the structures of the initial state (IS) and final state (FS)). Notably, the TS was confirmed by identifying an imaginary vibrational mode (Tables S6–S8). The TS was located at $d_{C-C}=1.9$ Å at all of the SCN sites. When the potential energy of the IS was set to zero, the activation barriers from the IS to the TS were estimated to be 0.85, 0.49, and 0.82 eV for SCN $=9$, SCN $=8$, and SCN $=7$, respectively. The local minimum energy appeared at 1.5 Å on SCN $=9$ and 8 and at 1.6 Å on SCN $=7$, corresponding to the adsorbed *OCCO intermediate. The thermodynamic energy of *OCCO was lower on SCN $=9$ (0.61 eV) and SCN $=8$ (0.22 eV) surfaces than on an SCN $=7$ surface (0.75 eV). The activation energy (i.e., the energy difference between the TS and FS) for the reverse reaction, which involves the splitting of *OCCO into two *CO, was 0.24, 0.27, and 0.07 eV for SCN $=9$, SCN $=8$, and SCN $=7$ surfaces, respectively. Therefore, at an SCN $=7$ surface, although the activation barrier for *OCCO formation was moderate compared with that of surfaces with higher SCN values, the resultant *OCCO was less stable and the activation barrier for the reverse reaction was lower. Consequently, the reverse reaction, where *OCCO dissociates, occurred rapidly, hindering progression to the subsequent intermediate reduction process at low-SCN sites. Moreover, the low SCN sites would exhibit high CO adsorption strength, which limits the mobility of CO on the Cu surface and hinders the CO dimerization.[28] This inference is supported by Figure S24c, which shows a sharp energy increase near $d_{C-C}=3.3$ Å. Mean-

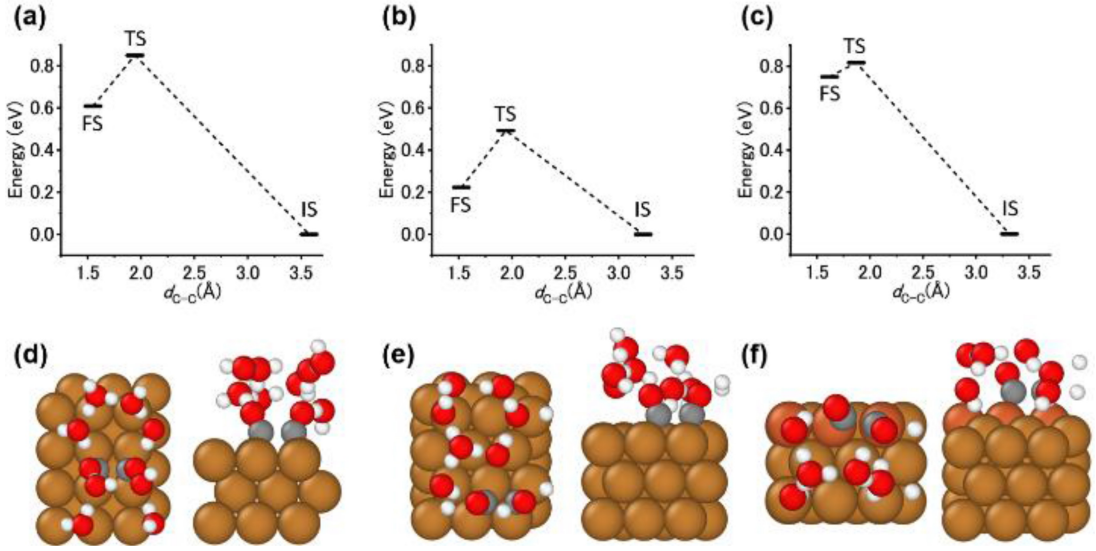

Figure 5. Energy diagram of CO dimerization on sites with (a) SCN = 9, (b) SCN = 8, and (c) SCN = 7. The structure of TS on the sites with (d) SCN = 9, (e) SCN = 8, and (f) SCN = 7 from the top and side. Gray, red, white, brown, and dark-orange spheres represent C, O, H, Cu, and Cu with SCN = 7, respectively.

while, since the activation energy for the CO dimerization was lower at SCN = 8 compared to SCN = 9, subsequent reaction intermediates are expected to be more likely to be observed, which is consistent with previous experimental studies.[46]

Discussion

On the basis of the obtained results, we discuss the size-dependent effects of the CuNCs on the CORR performance. Figure 6 shows a schematic of the CORR activity on the electrochemically grown CuNCs. At the same potential, larger CuNCs were observed in Cu-CTFs with higher Cu loading. According to CuNC models, larger CuNCs exhibit a higher proportion of SCN = 8 and 9, and DFT results suggest that the *OCCO, a key species for C_{2+} products, could stably exist on these sites. By contrast, smaller CuNCs in Cu-CTFs have a higher proportion of SCN = 7 and the experimental results confirmed the formation of smaller amounts of C_{2+} products. The DFT results indicate that the *OCCO is unstable on SCN = 7 sites, which explains the low production of C_{2+} products. Our results are basically consistent with a previous study demonstrating that larger CuNCs enhance the reduction of CO to C_{2+} under alkaline conditions.[19] Additionally, Smaller CuNPs (in the size range of 2–15 nm) produce only trace amounts of C_{2+} products ($FE_{C2H4} < 5\%$) during CO_2RR,[28] whereas our study demonstrated that even smaller CuNCs (< 1.0 nm) exhibited notable C_{2+} production (e.g., 29.5 % of FE_{C2+} with Cu(I)-CTFs at −0.8 V *vs.* RHE) during CORR. These findings suggest that even small CuNCs can generate C_{2+} products under high CO surface coverage conditions. However, it should be noted that the surface pH differs between CORR and CO_2RR. Therefore, when employing CuNCs for CO_2 electrolysis, increasing the partial pressure of CO through tandem integration with CO_2-to-CO

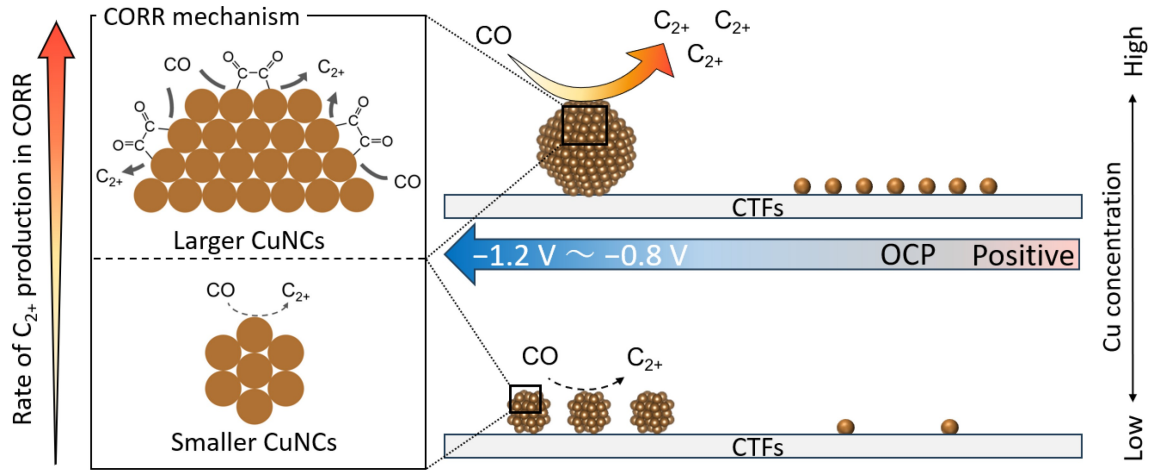

Figure 6. Schematic of CORR process on electrochemically grown CuNCs derived from single Cu atoms for lower and higher Cu concentration on the CTFs.

electrolysis or optimizing the catalyst layer structure would be an effective approach.

Conclusions

We systematically evaluated the correlation between CuNCs derived from single Cu-doped CTFs formed during CORR and their CORR activities. *Operando* XAFS analysis revealed that Cu clusters of several nanometers were grown under a cathodic potential and that their size increased with increasing Cu loading on the substrate and increasingly negative applied potential. The CORR results show that the amount and rate of C_{2+} formation increased, especially with increasing the size of CuNCs. To investigate the correlation between the CORR activity and the grown Cu cluster size, we modeled CuNCs a few nanometers in size. The modeling results indicated that the fraction of SCN < 8 decreased and that of SCN = 9 and 8 increased with increasing size. Combined with the EXAFS data, this result suggested that the exposed surfaces of larger Cu clusters formed when the Cu loading was increased, or more negative potentials were applied had a greater proportion of SCN = 9 and 8 than SCN < 8. We used the CI-NEB method to calculate the energy profiles of the CO dimerization reaction, which is an important elementary process in the formation of C_{2+} products, on each SCN site. Because of the high reverse reaction rate and thermodynamic instability of *OCCO at SCN = 7 sites, CO dimerization to C_{2+} production is more likely to occur at SCN = 9 and SCN = 8 sites. The insights gained from this study are expected to contribute to the advancement of Cu-based catalysts for the CO_2RR/CORR. In addition, we anticipate that these findings will enhance understanding of SACs, which exhibit unique reactions distinct from bulk catalysts.

Acknowledgments

This work was supported by the CREST (grant JPMJCR24S6) of the Japan Science and Technology Agency and the JSPS KAKENHI Program (grants 23KJ1438 and 23H02063). Static DFT calculations were partly achieved through the use of SQUID at the D3 Center, Osaka University. TEM measurement was carried out by using a facility in the Research Center for Ultra-High Voltage Electron Microscopy, Osaka University and TEM observation was supported by Dr. Takao Sakata. We also acknowledge Dr. Y. Hayasaka in Tohoku University for the STEM observation. Synchrotron radiation experiments were performed using the BL01B1 beamline of SPring-8 with approval of the Japan Synchrotron Radiation Research Institute (proposals 2023A1690, 2023A1934, 2023B2081, 2023B2097, 2024A1940).

Conflict of Interests

The authors declare no conflict of interest.

Data Availability Statement

The data that support the findings of this study are available from the corresponding author upon reasonable request.

Keywords: CO reduction reaction · C_{2+}products, Cu nanoclusters derived from single-atom catalysts · *Operando*XAFS · DFT calculations

[1] P. De Luna, C. Hahn, D. Higgins, S. A. Jaffer, T. F. Jaramillo, E. H. Sargent, *Science* **2019**, *364*.
[2] Z. W. Seh, J. Kibsgaard, C. F. Dickens, I. Chorkendorff, J. K. Nørskov, T. F. Jaramillo, *Science* **2017**, *355*.
[3] G. Wang, J. Chen, Y. Ding, P. Cai, L. Yi, Y. Li, C. Tu, Y. Hou, Z. Wen, L. Dai, *Chem. Soc. Rev.* **2021**, *50*, 4993–5061.
[4] A. R. Woldu, Z. Huang, P. Zhao, L. Hu, D. Astruc, *Coord. Chem. Rev.* **2022**, *454*, 214340–214368.
[5] B. Chang, H. Pang, F. Raziq, S. Wang, K.-W. Huang, J. Ye, H. Zhang, *Energy Environ. Sci.* **2023**, *16*, 4714–4758.
[6] K. Zhao, X. Quan, *ACS Catal.* **2021**, *11*, 2076–2097.
[7] M. Jouny, G. S. Hutchings, F. Jiao, *Nat. Catal.* **2019**, *2*, 1062–1070.
[8] M. G. Kibria, J. P. Edwards, C. M. Gabardo, C. T. Dinh, A. Seifitokaldani, D. Sinton, E. H. Sargent, *Adv. Mater.* **2019**, *31*, e1807166.
[9] S. Liang, N. Altaf, L. Huang, Y. Gao, Q. Wang, *J. CO2 Util.* **2020**, *35*, 90–105.
[10] A. Inoue, T. Harada, S. Nakanishi, K. Kamiya, *EES Catal.* **2023**, *1*, 9–16.
[11] Y. Hori, A. Murata, R. Takahashi, S. Suzuki, *Chem. Lett.* **1987**, *16*, 1665–1668.
[12] Y. Hori, A. Murata, R. Takahashi, *J. Chem. Soc. Faraday Trans.* **1989**, *85*, 2309–2326.
[13] A. Bagger, W. Ju, A. S. Varela, P. Strasser, J. Rossmeisl, *ChemPhysChem* **2017**, *18*, 3266–3273.
[14] Y. Zheng, A. Vasileff, X. Zhou, Y. Jiao, M. Jaroniec, S. Z. Qiao, *J. Am. Chem. Soc.* **2019**, *141*, 7646–7659.
[15] K. Zhao, X. Nie, H. Wang, S. Chen, X. Quan, H. Yu, W. Choi, G. Zhang, B. Kim, J. G. Chen, *Nat. Commun.* **2020**, *11*, 2455.
[16] H. Bao, Y. Qiu, X. Peng, J. A. Wang, Y. Mi, S. Zhao, X. Liu, Y. Liu, R. Cao, L. Zhuo, J. Ren, J. Sun, J. Luo, X. Sun, *Nat. Commun.* **2021**, *12*, 238.
[17] X. F. Qiu, H. L. Zhu, J. R. Huang, P. Q. Liao, X. M. Chen, *J. Am. Chem. Soc.* **2021**, *143*, 7242–7246.
[18] X. F. Qiu, J. R. Huang, C. Yu, Z. H. Zhao, H. L. Zhu, Z. Ke, P. Q. Liao, X. M. Chen, *Angew. Chem. Int. Ed.* **2022**, *61*, e202206470.
[19] W. Rong, H. Zou, W. Zang, S. Xi, S. Wei, B. Long, J. Hu, Y. Ji, L. Duan, *Angew. Chem. Int. Ed.* **2021**, *60*, 466–472.
[20] C. E. Creissen, M. Fontecave, *Nat. Commun.* **2022**, *13*, 2280.
[21] Z. Weng, Y. Wu, M. Wang, J. Jiang, K. Yang, S. Huo, X. F. Wang, Q. Ma, G. W. Brudvig, V. S. Batista, Y. Liang, Z. Feng, H. Wang, *Nat. Commun.* **2018**, *9*, 415.
[22] Y. Xu, F. Li, A. Xu, J. P. Edwards, S. F. Hung, C. M. Gabardo, C. P. O'Brien, S. Liu, X. Wang, Y. Li, J. Wicks, R. K. Miao, Y. Liu, J. Li, J. E. Huang, J. Abed, Y. Wang, E. H. Sargent, D. Sinton, *Nat. Commun.* **2021**, *12*, 2932.
[23] L. Ma, W. Hu, B. Mei, H. Liu, B. Yuan, J. Zang, T. Chen, L. Zou, Z. Zou, B. Yang, Y. Yu, J. Ma, Z. Jiang, K. Wen, H. Yang, *ACS Catal.* **2020**, *10*, 4534–4542.
[24] L. Yan, X. D. Liang, Y. Sun, L. P. Xiao, B. A. Lu, G. Li, Y. Y. Li, Y. H. Hong, L. Y. Wan, C. Chen, J. Yang, Z. Y. Zhou, N. Tian, S. G. Sun, *Chem. Commun.* **2022**, *58*, 2488–2491.
[25] D. Karapinar, N. T. Huan, N. Ranjbar Sahraie, J. Li, D. Wakerley, N. Touati, S. Zanna, D. Taverna, L. H. Galvao Tizei, A. Zitolo, F. Jaouen, V. Mougel, M. Fontecave, *Angew. Chem. Int. Ed.* **2019**, *58*, 15098–15103.
[26] T. Liu, H. Yabu, *EcoEnergy* **2024**, *2*, 419–432.
[27] D. Hursan, J. Timoshenko, E. Ortega, H. S. Jeon, M. Ruscher, A. Herzog, C. Rettenmaier, S. W. Chee, A. Martini, D. Koshy, B. Roldan Cuenya, *Adv. Mater.* **2024**, *36*, e2307809.
[28] R. Reske, H. Mistry, F. Behafarid, B. Roldan Cuenya, P. Strasser, *J. Am. Chem. Soc.* **2014**, *136*, 6978–6986.
[29] K. Iwase, T. Yoshioka, S. Nakanishi, K. Hashimoto, K. Kamiya, *Angew. Chem. Int. Ed.* **2015**, *54*, 11068–11072.
[30] P. Su, K. Iwase, T. Harada, K. Kamiya, S. Nakanishi, *Chem. Sci.* **2018**, *9*, 3941–3947.

[31] T. Yoshioka, K. Iwase, S. Nakanishi, K. Hashimoto, K. Kamiya, *J. Phys. Chem. C* **2016**, *120*, 15729–15734.
[32] K. Kamiya, R. Kamai, K. Hashimoto, S. Nakanishi, *Nat. Commun.* **2014**, *5*, 5040.
[33] S. Kato, K. Iwase, T. Harada, S. Nakanishi, K. Kamiya, *ACS Appl. Mater. Interfaces* **2020**, *12*, 29376–29382.
[34] K. Kamiya, *Chem. Sci.* **2020**, *11*, 8339–8349.
[35] S. Kato, T. Hashimoto, K. Iwase, T. Harada, S. Nakanishi, K. Kamiya, *Chem. Sci.* **2023**, *14*, 613–620.
[36] X. Liu, J. Xiao, H. Peng, X. Hong, K. Chan, J. K. Nørskov, *Nat. Commun.* **2017**, *8*, 15438.
[37] L. Wang, S. A. Nitopi, E. Bertheussen, M. Orazov, C. G. Morales-Guio, X. Liu, D. C. Higgins, K. Chan, J. K. Nørskov, C. Hahn, T. F. Jaramillo, *ACS Catal.* **2018**, *8*, 7445–7454.
[38] L. Xiong, X. Zhang, L. Chen, Z. Deng, S. Han, Y. Chen, J. Zhong, H. Sun, Y. Lian, B. Yang, X. Yuan, H. Yu, Y. Liu, X. Yang, J. Guo, M. H. Rummeli, Y. Jiao, Y. Peng, *Adv. Mater.* **2021**, *33*, e2101741.
[39] X. Peng, X. Chen, Y. Zhou, F. Sun, T. Zhang, L. Zheng, L. Jiang, X. Wang, *J. Catal.* **2022**, *408*, 98–108.
[40] Y. Lum, T. Cheng, W. A. Goddard III, J. W. Ager, *J. Am. Chem. Soc.* **2018**, *140*, 9337–9340.
[41] J. H. Montoya, C. Shi, K. Chan, J. K. Nørskov, *J. Phys. Chem. Lett.* **2015**, *6*, 2032–2037.
[42] L. Fan, C. Xia, F. Yang, J. Wang, H. Wang, Y. Lu, *Sci. Adv.* **2020**, *6*, eaay3111.
[43] W. Deng, P. Zhang, Y. Qiao, G. Kastlunger, N. Govindarajan, A. Xu, I. Chorkendorff, B. Seger, J. Gong, *Nat. Commun.* **2024**, *15*, 892.
[44] W. Rong, H. Zou, S. Tan, E. Hu, F. Li, C. Tang, H. Dai, S. Wei, Y. Ji, L. Duan, *CCS Chem.* **2023**, *5*, 1176–118.
[45] R. B. Sandberg, J. H. Montoya, K. Chan, J. K. Nørskov, *Surf. Sci.* **2016**, *654*, 56–62.
[46] E. Perez-Gallent, M. C. Figueiredo, F. Calle-Vallejo, M. T. Koper, *Angew. Chem. Int. Ed.* **2017**, *56*, 3621–3624.

Manuscript received: December 3, 2024
Revised manuscript received: January 24, 2025
Accepted manuscript online: January 24, 2025
Version of record online: ■■, ■■